Published for the International Glaciological Society

Improved representation of laminar and turbulent sheet flow in subglacial drainage models

Journal:	*Journal of Glaciology*
Manuscript ID	JOG-23-0077
Manuscript Type:	Article
Date Submitted by the Author:	22-Jun-2023
Complete List of Authors:	Hill, Tim; Simon Fraser University, Earth Sciences Flowers, Gwenn; Simon Fraser University, Earth Sciences Hoffman, Matthew; Los Alamos National Laboratory, Fluid Dynamics and Solid Mechanics Group Bingham, Derek; Simon Fraser University, Department of Statistics and Actuarial Science Werder, Mauro; ETH Zurich Campus Honggerberg, BAUG
Keywords:	Glacier hydrology, Glacier modelling, Subglacial processes
Abstract:	Subglacial hydrology models struggle to reproduce seasonal drainage patterns that are consistent with observed subglacial water pressures and surface velocities. We modify the standard sheet-flow parameterization within a coupled sheet--channel subglacial drainage model to smoothly transition between laminar and turbulent flow based on the locally computed Reynolds number in a physically consistent way (the “transition”' model). We compare the transition model to standard laminar and turbulent models to assess the role of the sheet-flow parameterization in reconciling observed and modelled water pressures under idealized and realistic forcing. Relative to the turbulent model, the laminar and transition models improve seasonal simulations in four distinct ways: they (1) increase winter water pressure by 25--35%, (2) produce late-summer water pressure below the winter baseline, (3) decrease the peak spring water pressure, and (4) reduce the duration of water pressure exceeding overburden. In contrast to the laminar model,

	the transition model remains consistent with its own internal assumptions across all flow regimes. Based on the improved performance and internal consistency of the transition model, we recommend its use for transient simulations of subglacial drainage.

Journal of Glaciology, Vol. 00, No. 0, 0000

Improved representation of laminar and turbulent sheet flow in subglacial drainage models

Tim Hill[1], Gwenn E. Flowers[1], Matthew J. Hoffman[2], Derek Bingham[3], Mauro A. Werder[4,5]

[1]*Department of Earth Sciences, Simon Fraser University, Burnaby, BC, Canada*

[2]*Fluid Dynamics and Solid Mechanics Group, Los Alamos National Laboratory, Los Alamos, NM, USA*

[3]*Department of Statistics and Actuarial Science, Simon Fraser University, Burnaby, BC, Canada*

[4]*Laboratory of Hydraulics, Hydrology and Glaciology (VAW), ETH Zurich, Zurich, Switzerland*

[5]*Swiss Federal Institute for Forest, Snow and Landscape Research (WSL), Birmensdorf, Switzerland*

Correspondence: Tim Hill <tim_hill_2@sfu.ca>

ABSTRACT.

Subglacial hydrology models struggle to reproduce seasonal drainage patterns that are consistent with observed subglacial water pressures and surface velocities. We modify the standard sheet-flow parameterization within a coupled sheet–channel subglacial drainage model to smoothly transition between laminar and turbulent flow based on the locally computed Reynolds number in a physically consistent way (the "transition" model). We compare the transition model to standard laminar and turbulent models to assess the role of the sheet-flow parameterization in reconciling observed and modelled water pressures under idealized and realistic forcing. Relative to the turbulent model, the laminar and transition models improve seasonal simulations in four distinct ways: they (1) increase winter water pressure by 25–35%, (2) produce late-summer water pressure below the winter baseline, (3) decrease the peak spring water pressure, and (4) reduce the duration of water pressure exceeding overburden. In contrast to the laminar model, the transition model remains consistent with its own internal assumptions across all flow regimes. Based on the improved performance and internal consistency of the transition model, we recommend its use for transient simulations of subglacial drainage.

1 INTRODUCTION

The subglacial drainage system beneath the flanks of the Greenland Ice Sheet is subject to seasonal variations in surface melt input, resulting in strong seasonal cycles in subglacial water pressure and ice flow (e.g., Joughin and others, 2008; Moon and others, 2014; Davison and others, 2020; Vijay and others, 2021). The seasonal velocity patterns, and how they vary with increasing volumes of surface melt, are key to understanding ice-discharge-related sea-level contributions from Greenland (e.g., King and others, 2020). However, it remains difficult to model seasonal water pressure and corresponding ice-flow velocities (e.g., Koziol and Arnold, 2018; Cook and others, 2022; Ehrenfeucht and others, 2023) that are consistent with observations of water pressure and ice velocity (e.g., Andrews and others, 2014; Moon and others, 2014; Nienow and others, 2017), limiting the ability of existing models to explain ice-flow patterns and their seasonal variations.

Modern subglacial hydrology models represent water flow through a variety of flow elements, most commonly including efficient drainage through R-channels (Röthlisberger, 1972) and inefficient drainage through linked cavities (Kamb, 1987). Models take different forms (e.g., Flowers, 2015), including those with coupled distributed–channelized flow and spatially extensive channel networks (e.g., Werder and others, 2013; Hewitt, 2013; Hoffman and others, 2018), as well as those comprised of a single set of flow elements that transition between inefficient and efficient drainage (Schoof, 2010; Sommers and others, 2018; Felden and others, 2023). Some models represent physical processes in more detail, for example by including a weakly connected drainage system (e.g., Hoffman and others, 2016), while others trade process detail for computational efficiency (e.g., de Fleurian and others, 2014; Bueler and van Pelt, 2015).

Models that explicitly represent distributed and channelized flow elements (e.g., Werder and others, 2013; Hewitt, 2013; Hoffman and others, 2018) capture much of the presently understood physics of real subglacial drainage and have had success when applied to steady-state ice-sheet hydrology (e.g., Hager and others, 2022), with modelled drainage pathways resembling those inferred from radar data (e.g., Dow and others, 2020). However, these models have difficulty producing realistic water-pressure variations when applied to ice-sheet-scale domains and forced with seasonally varying surface melt inputs. Specifically, models tend to (1) underpredict winter water pressures (de Fleurian and others, 2018; Poinar and others, 2019; Ehrenfeucht and others, 2023) compared to winter water pressure inferred from seasonal velocity patterns (e.g., Moon and others, 2014; Vijay and others, 2021) and observed in borehole water pressures (e.g., Andrews and others, 2014; Wright and others, 2016) (c.f., Downs and others, 2018), (2) fail to capture the late-summer pressure minimum (e.g., Koziol and Arnold, 2018; Cook and others, 2020) that is inferred from typical Greenland outlet glacier velocity records (e.g., Davison and others, 2020), (3) predict unrealistically large spring pressure peaks exceeding overburden (e.g., Werder and others, 2013; Banwell and others, 2016; Poinar and others, 2019; de Fleurian and others, 2018) that sometimes necessitate capping minimum effective pressures in dynamically coupled simulations (e.g., Ehrenfeucht and others, 2023) and render water pressure insensitive to melt rate variations (Koziol and Arnold, 2018), and (4) require a priori assumptions about distributed flow being fully laminar or turbulent (e.g., Werder and others, 2013; Hewitt, 2013). It is unclear whether the assumptions in (4) hold across the typical spatiotemporal domain of these models. Resolving the discrepancies enumerated above is important for capturing the complete relationship between surface melt, subglacial drainage, and ice flow in numerical models.

Most subglacial drainage models require specification of the relationship between water flux or discharge and the hydraulic potential gradient driving flow at the scale of drainage elements. Here we investigate the role of this relationship within distributed drainage components in controlling seasonal pressure variations as modelled with the Glacier Drainage System (GlaDS) model (Werder and others, 2013), a representative example of an explicitly channel-resolving model. We compare seasonal water-pressure variations modelled for different flux models to assess the influence on the shortcomings identified above. On the basis of our results, we make recommendations for the parameterization of distributed water flux in this popular class of channel-resolving drainage models.

2 METHODS

2.1 Subglacial hydrology model

Subglacial drainage is modelled with the Glacier Drainage System (GlaDS) model (Werder and others, 2013) as implemented in MATLAB (version tag `v1.0.0-transition`). GlaDS conceptualizes subglacial water flow occurring through a distributed drainage system composed of linked cavities and through an efficient drainage system composed of R-channels (Schoof and others, 2012; Hewitt and others, 2012; Werder and others, 2013). GlaDS is a representative example of the broader class of multi-component models that share common physical processes (e.g., Hewitt, 2013; Hoffman and others, 2018), and primarily differs in the discrete nature of subglacial channels from models that represent individual elements as transitioning between distributed and channelized flow (e.g., Schoof, 2010; Sommers and others, 2018; Felden and others, 2023).

GlaDS requires specification of a number of parameters that control the formation of subglacial cavities, water flow within distributed and channelized drainage elements, basal sliding, englacial water storage, and the strength of sheet–channel coupling. Constraining drainage model parameters with direct measurements is difficult and has only rarely been done for a few model parameters (e.g., Werder and others, 2009; Pohle and others, 2022). Inferring parameters via drainage model inversions has recently been demonstrated (e.g., Irarrazaval and others, 2021; Brinkerhoff and others, 2021), however, observational data density will likely remain insufficient to constrain all parameters. In this study, model parameter values (Table 1) are chosen to obtain summer water pressures near overburden with widespread channelization. These values are similar to existing model applications to Greenland-scale catchments with seasonal melt forcing (e.g., Gagliardini and Werder, 2018; Downs and others, 2018; Cook and others, 2022). The size of the controlling bed obstacle (including both the bump height $h_{\rm b}$ and the bump length $l_{\rm b}$), the width of sheet flow contributing to channel discharge ($l_{\rm c}$), and the channel conductivity ($k_{\rm c}$) in particular are larger here than typically used for alpine glaciers (e.g., Werder and others, 2013) or steady state Antarctic applications (e.g., Dow and others, 2022; Hager and others, 2022), potentially reflecting the physically larger scale compared to alpine glaciers and the increased size of drainage elements compared to Antarctic applications.

We intentionally disallow cavities from opening by ice creep when water pressure exceeds ice overburden by setting the ice creep constant $\tilde{A}_{\rm s} = 0$ when $p_{\rm w} > p_{\rm i}$. We expect that unrepresented physical mechanisms would take over when $p_{\rm w}$ exceeds $p_{\rm i}$ (e.g., Tsai and Rice, 2010; Schoof and others, 2012; Dow and others, 2015). Based on model experiments, allowing cavities to creep open as a rough approximation of these mechanisms leads to undesirable behaviour: cavities grow arbitrarily large within overpressurized regions, preventing channels from developing and leading to persistent and extensive pressure above overburden. Disabling creep opening is therefore a suitable modelling choice for the configuration presented here.

While GlaDS is a representative example of a channel-resolving subglacial drainage model, there are physical processes that are missing in its formulation, especially the representation of hydraulically unconnected or weakly connected bed patches (e.g., Murray and Clarke, 1995; Andrews and others, 2014; Hoffman and others, 2016). Since GlaDS represents only hydraulically connected drainage, winter water pressures may be expected to be lower than observations of winter water pressure within disconnected patches. For example, Rada Giacaman and Schoof (2023) report mean winter water pressure ∼90% of overburden within hydraulically connected boreholes and > 100% of overburden for hydraulically unconnected boreholes for

Table 1. Constants (top group) and model parameters (bottom group) for GlaDS simulations.

Symbol	Description	Value	Units
ρ_{w}	Density of water	1000	kg m^{-3}
ρ_{i}	Density of ice	910	kg m^{-3}
g	Gravitational acceleration	9.81	m^{3} s^{-1}
c_{w}	Specific heat capacity of water	4.22×10^{3}	J kg^{-1}
c_{t}	Pressure melting coefficient	-7.50×10^{-8}	K Pa^{-1}
ν	Kinematic viscosity of water at 0°C	1.793×10^{-6}	m s^{-2}
k_{s}	Effective laminar sheet conductivity	0.1	Pa s^{-1}
α_{s}	Sheet-flow exponent	$[\frac{5}{4}, \frac{3}{2}, 3]$	
β_{s}	Sheet-flow exponent	$[\frac{3}{2}, 2]$	
k_{c}	Channel conductivity	0.2	m$^{3/2}$s^{-1}
α_{c}	Channel-flow exponent	5/4	
β_{c}	Channel-flow exponent	3/2	
h_{b}	Bed bump height	0.5	m
l_{b}	Bed bump length	10	m
l_{c}	Width of sheet-flow contributing to channel	10	m
e_{v}	Englacial porosity	1×10^{-4}	
ω	Laminar–turbulent transition parameter	1/2000	
u_{b}	Basal velocity	30	m a^{-1}
$\tilde{A}^{a}$	Rheological parameter for creep closure	1.78×10^{-25}	s^{-1} Pa^{-3}
$\tilde{A}_{\mathrm{s}}$	Rheological parameter for creep when $N < 0$	0	s^{-1} Pa^{-3}
n	Ice-flow exponent	3	
$\dot{m}_{\mathrm{s}}$	Basal melt rate	0.01	m w.e. a^{-1}

[a] $\tilde{A}$ differs from the canonical rheology parameter A by a factor of $\frac{2}{27}$. The listed value for $\tilde{A}$ corresponds to the recommended value $A = 2.4 \times 10^{-24}$ s^{-1} Pa^{-3} for temperate ice (Cuffey and Paterson, 2010)

a small alpine glacier.

2.2 Sheet-flow model

Progress has been made in addressing the shortcomings listed above through adjustments to the distributed drainage flow parameterization, including representing flow within the distributed drainage system as laminar (Hewitt, 2013; Banwell and others, 2016; Gagliardini and Werder, 2018; Cook and others, 2022), by explicitly parameterizing hydraulic conductivity as a function of surface melt rate (e.g., Downs and others, 2018) or by including a Reynolds-number-dependent transmissivity (Sommers and others, 2018). These models share the common feature that resistance to water flow in the distributed drainage system is sensitive to the volume of water supplied to the subglacial system. This sensitivity is obtained in different ways, but with similar impacts on the modelled winter water pressure.

2.2.1 Standard sheet-flow model

We consider two primary forms for the distributed water flux parameterization with GlaDS. The standard discharge-per-unit-width parameterization for subglacial drainage models intends to represent the average flux through many sub-grid-scale linked cavities (e.g., Werder and others, 2013; Hewitt, 2013; Hoffman and others, 2018) and can be written

$$\mathbf{q} = -k_\mathrm{s} h^{\alpha_\mathrm{s}} |\nabla\phi|^{\beta_\mathrm{s}-2}\nabla\phi, \tag{1}$$

for conductivity k_s, water thickness h, hydraulic potential ϕ, and exponents α_s and β_s.

Choosing values for α_s and β_s requires an assumption about the relationship between water flux, cavity height, and the hydraulic potential gradient. Values of $\alpha_\mathrm{s} = 3$ and $\beta_\mathrm{s} = 2$ correspond to purely laminar flow (e.g., Creyts and Schoof, 2009; Hewitt, 2013; Cook and others, 2022), while $\alpha_\mathrm{s} = 5/4$ and $\beta_\mathrm{s} = 3/2$ are typically explained as representing fully turbulent flow according to the Darcy–Weisbach relationship (e.g., Schoof and others, 2012; Werder and others, 2013; Hoffman and others, 2018). It is worth noting that the parameterization for channel discharge is written in an analogous way, with the same interpretation of the exponents α_c and β_c.

The validity of the laminar or turbulent assumption can be assessed by inspecting the Reynolds number, Re. In the context of standard fluid dynamics, the Reynolds number predicts whether a specified flow is laminar or turbulent. For a general flow with representative velocity V, length scale D, and for a fluid with kinematic viscosity ν, the Reynolds number is the ratio of the inertial and viscous forces, $\mathrm{Re} = \frac{VD}{\nu}$. In the context of the discharge-per-unit-width parameterization (Eq. 1), the length scale D is set to the water sheet thickness h, so the Reynolds number becomes $\mathrm{Re} = \frac{q}{\nu}$.

The transition between laminar and turbulent flow is best understood for the simple case of flow through circular pipes. In this case, the empirical relationship between Re and the Darcy friction factor f_{D} is summarized by the Moody diagram (Moody, 1944), which demonstrates the clear differences in the behaviour of laminar and turbulent flows (Fig. 1). Laminar flow results in an inverse relationship between Re and f_{D} that is independent of roughness (straight line in Fig. 1). Fully turbulent flow is represented by the friction factor being independent of Re as $\mathrm{Re} \to \infty$. The transition from laminar to fully turbulent flow can be approximated by the Colebrook–White equation (Colebrook and White, 1937).

The fully turbulent behaviour from the Moody diagram can be carried over to the context of distributed subglacial water flow through a macroporous sheet by writing the Darcy–Weisbach equation (e.g., Moody, 1944) for flow between parallel plates and in terms of the flux q instead of the flow velocity. By doing this, fully turbulent flow would require a flow exponent $\alpha_{\mathrm{s}} = 3/2$, as in the SHAKTI model (Sommers and others, 2018) and in contrast to the assumed value of 5/4 for GlaDS and similar models; however, given the conceptual differences between flow through rough pipes, on which the Moody diagram is based, and the subglacial linked cavity system, we test the sensitivity of modelled water pressure to turbulent flow exponent values $\alpha_{\mathrm{s}} = 3/2$ and $\alpha_{\mathrm{s}} = 5/4$. We denote the model using Eq. (1) with $\alpha_{\mathrm{s}} = 5/4$ "turbulent 5/4", with $\alpha_{\mathrm{s}} = 3/2$ "turbulent 3/2", and with $\alpha_{\mathrm{s}} = 3$ and $\beta_{\mathrm{s}} = 2$ as "laminar" (Table 2). All models use $\beta_{\mathrm{s}} = 3/2$ to represent turbulent flow.

2.2.2 Sheet-flow model with laminar–turbulent transitions

Equation (1) assumes that water flow everywhere and at all times is either purely laminar or purely turbulent. To remove this limitation and develop a model appropriate for the entire Re range, we replace Eq. (1) with a model that represents both laminar and turbulent flow, with the partitioning governed by the local Reynolds number:

$$-k_{\mathrm{s}} h^3 \nabla \phi = \mathbf{q} + \omega \mathrm{Re} \left(\frac{h}{h_b} \right)^{3-2\alpha_{\mathrm{s}}} \mathbf{q}, \tag{2}$$

for bed bump height h_{b}. Substituting $\mathrm{Re} = \frac{q}{\nu}$ yields a quadratic equation that can be solved exactly for q. The transition parameter ω governs partitioning between laminar and turbulent flow, with the transition

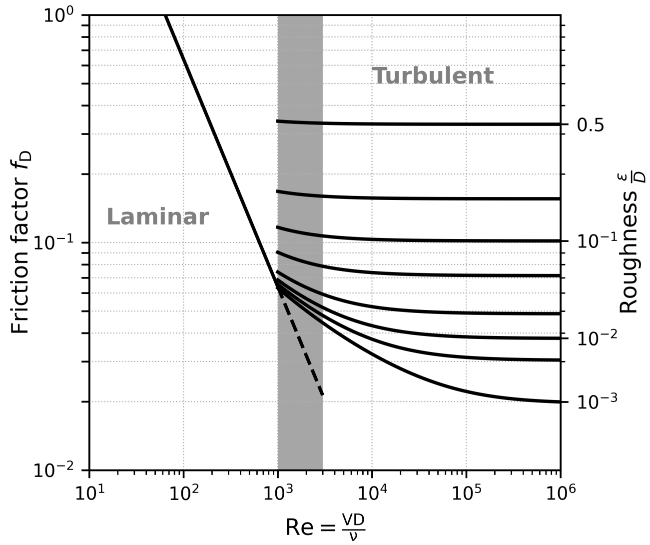

Fig. 1. Moody diagram, representing the friction factor $f_\mathrm{D} = \frac{h_\mathrm{l}}{\left(\frac{L}{D}\right)\frac{V^2}{2g}}$ (for head loss h_l over a pipe of length L, diameter D, and with flow velocity V), as a function of the Reynolds number $\mathrm{Re} = \frac{\mathrm{VD}}{\nu}$ for different relative roughness scales (ε). The transition region (shaded grey, $1000 \leq \mathrm{Re} \leq 3000$) separates regions of laminar flow and turbulent flow. The laminar friction factor is $f_\mathrm{D} = \frac{64}{\mathrm{Re}}$ (Moody, 1944), and the friction factor in the transition and turbulent regimes is computed using the Colebrook-White equation (Colebrook and White, 1937).

occuring at approximately $\mathrm{Re} = 1/\omega$. The exponent α_s controls the behaviour of the model in the fully turbulent limit ($\omega\mathrm{Re} \gg 1$).

We call Eq. (2), which transitions between laminar and turbulent flow based on the local Reynolds number, the "transition" model. In the laminar regime ($\omega\mathrm{Re} \ll 1$), the first term on the right hand side dominates and Eq. (2) reduces to the laminar model (Eq. 1 with $\alpha_\mathrm{s} = 3$ and $\beta_\mathrm{s} = 2$). In the turbulent regime ($\omega\mathrm{Re} \gg 1$), the second term on the right hand side dominates and Eq. (2) reduces to the turbulent model (Eq. 1 with α_s specified by the turbulent assumption and $\beta_\mathrm{s} = 3/2$) with an effective turbulent conductivity given by $k_\mathrm{t}^2 = k_\mathrm{s}\frac{\nu}{\omega}h_\mathrm{b}^{3-2\alpha_\mathrm{s}}$. In the intermediate regime ($\omega\mathrm{Re} \sim 1$), Eq. (2) smoothly blends laminar and turbulent flow. Table 2 summarizes the five flux parameterizations obtained by applying Eqs. (1) and (2) with turbulent flow exponents $\alpha_\mathrm{s} = 5/4$ and $\alpha_\mathrm{s} = 3/2$.

Figure 2 compares the flux dependence on sheet thickness for the transition (Eq. 2), laminar and turbulent models (Eq. 1) for a fixed hydraulic potential gradient. The nondimensional sheet thickness, $\tilde{h} = \frac{h}{h_\mathrm{crit}}$, is scaled using the critical sheet thickness, defined as the sheet thickness that produces the critical Reynolds number ($\omega\mathrm{Re} = 1$). That is, h_crit is defined to satisfy

$$1 = \frac{\omega}{\nu}k_\mathrm{s}h_\mathrm{crit}^3\overline{\nabla\phi}, \tag{3}$$

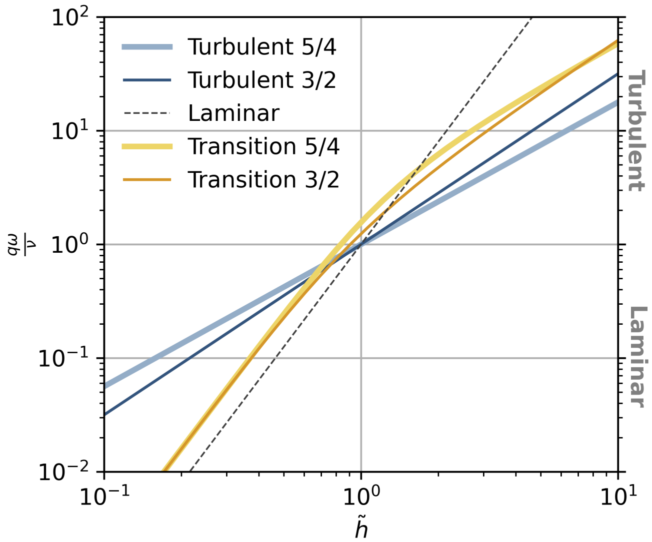

Fig. 2. Scaled sheet thickness $\tilde{h} = \frac{h}{h_{\mathrm{crit}}}$ and scaled sheet discharge $\frac{q\omega}{\nu}$ for the five flux parameterizations in Table 2 and with a fixed hydraulic potential gradient. The sheet thickness is scaled by h_{crit}, the sheet thickness that produces a Reynolds number equal to the transition threshold ($\omega\mathrm{Re} = 1$) for turbulent and laminar models.

where $\overline{\nabla\phi}$ is the mean hydraulic potential gradient assuming water pressure is equal to overburden for a given ice geometry. Equation (3) is derived from the laminar model, but with the sheet conductivity chosen for the turbulent model (Section 2.2.3), the critical sheet thickness is identical for laminar and turbulent models. Sheet flux is represented by $\omega\mathrm{Re} = \frac{q\omega}{\nu}$, such that values < 1 correspond to laminar flow and values > 1 represent turbulent flow.

Transitioning between laminar and turbulent flow in this way means that Eq. (2) has similar behaviour as that seen on the Moody diagram (Fig. 1). The flux is more sensitive to changes in cavity height h and potential gradient $\nabla\phi$ in the laminar regime than in the turbulent regime. By changing the sensitivity to h and $\nabla\phi$ as a function of Re, the transition model (Eq. 2) should allow for restricted flow during winter compared to a turbulent model. If the Reynolds number reaches or exceeds the transition point (set by $1/\omega$), the flux becomes less sensitive to h and $\nabla\phi$, such that the minimum flow resistance (measured by the friction factor f_{D}) is set by the fully turbulent limit, in contrast to the laminar model where there is no lower bound on the friction factor (e.g., the "Turbulent" region of the Moody diagram; Fig. 1).

The transition parameterization (Eq. 2) is similar in form to the Forchheimer equation used for non-Darcy flow through porous media, where the potential gradient is balanced by the sum of a linear term (with respect to flux, or equivalently velocity) representing laminar flow, and a quadratic term representing turbulent flow (e.g., Ward, 1964; Bear, 1972; Venkataraman and Rao, 1998). In the glaciological context, Stone

Table 2. Summary of sheet-flow parameterizations with parameter values substituted in the general forms (Eq. 1 and 2).

Model	Equation	Equation number	Parameters
Turbulent 5/4	$\mathbf{q} = -k_\mathrm{s} h^{5/4} \lvert\nabla\phi\rvert^{-1/2}\nabla\phi$	(1)	$\alpha_\mathrm{s} = 5/4$, $\beta_\mathrm{s} = 3/2$
Turbulent 3/2	$\mathbf{q} = -k_\mathrm{s} h^{3/2} \lvert\nabla\phi\rvert^{-1/2}\nabla\phi$	(1)	$\alpha_\mathrm{s} = 3/2$, $\beta_\mathrm{s} = 3/2$
Laminar	$\mathbf{q} = -k_\mathrm{s} h^{3} \nabla\phi$	(1)	$\alpha_\mathrm{s} = 3$, $\beta_\mathrm{s} = 2$
Transition 5/4	$\mathbf{q} = -\frac{\nu}{2\omega}\left(\frac{h_\mathrm{b}}{h}\right)^{1/2}\left(-1+\sqrt{1+4\frac{\omega}{\nu}\left(\frac{h}{h_\mathrm{b}}\right)^{1/2} k_\mathrm{s} h^3 \lvert\nabla\phi\rvert}\right)\frac{\nabla\phi}{\lvert\nabla\phi\rvert}$	(2)	$\alpha_\mathrm{s} = 5/4$
Transition 3/2	$\mathbf{q} = -\frac{\nu}{2\omega}\left(-1+\sqrt{1+4\frac{\omega}{\nu} k_\mathrm{s} h^3 \lvert\nabla\phi\rvert}\right)\frac{\nabla\phi}{\lvert\nabla\phi\rvert}$	(2)	$\alpha_\mathrm{s} = 3/2$

and Clarke (1993) applied the Forchheimer equation to represent drainage within till beneath Trapridge Glacier. The result of Eq. (2) has a similar effect as the Flowers and Clarke (2002) model, where hydraulic conductivity is a non-linearly increasing function of water thickness, such that the flux parameterization accommodates a large range in flux magnitudes and approximates both laminar and turbulent flows. Equation (2) is most closely related to the flux parameterization used by the SHAKTI (Sommers and others, 2018) and SUHMO (Felden and others, 2023) models. However, compared to SHAKTI and SUHMO, we apply this parameterization to represent flow exclusively within the distributed drainage system, whereas Sommers and others (2018) and Felden and others (2023) apply a similar parameterization to represent flow within the drainage system as a whole. We have further introduced a free conductivity parameter k_s to the transition model (Eq. 2) in order to recover the standard GlaDS model in laminar and turbulent limits. We retain the standard turbulent flux parameterization for subglacial channels (Werder and others, 2013, Eq. 12).

2.2.3 Turbulent model sheet conductivity

The turbulent models in Table 2 prescribe the conductivity k_s in units that depend on the value of α_s, and differ from the units of k_s in the laminar and transition models. The conductivity for the turbulent models must therefore be scaled appropriately to obtain a fair comparison between models. The conductivity for the turbulent models, k_t, is computed by setting the turbulent and laminar flux models equal with $h = h_\mathrm{crit}$ (Eq. 3) and with the mean hydraulic potential gradient (allowing for $\alpha_\mathrm{s} = 3/2$ or $5/4$ for the turbulent model),

$$k_\mathrm{t} h_\mathrm{crit}^{\alpha_\mathrm{s}} \overline{\lvert\nabla\phi\rvert}^{1/2} = k_\mathrm{s} h_\mathrm{crit}^{3} \overline{\lvert\nabla\phi\rvert}. \tag{4}$$

This scaling choice sets the laminar and turbulent models to intersect at $h = h_{\mathrm{crit}}$ and $\omega\mathrm{Re} = 1$ in Fig. 2. The turbulent models could, instead, be set to match the trajectory of the transition model in the fully turbulent limit. Matching the turbulent trajectories, however, would result in the turbulent models significantly overestimating sheet flux relative to the transition and laminar models for the entire range shown in Fig. 2, rendering the models incomparable. A similar scaling could be done to set the transition model to intersect the laminar and turbulent models at $h = h_{\mathrm{crit}}$ and $\omega\mathrm{Re} = 1$; however, we have chosen to match the laminar and transition models in the laminar regime (the slight offset in Fig. 2 for $\tilde{h} < 1$ represents the small contribution of the second term in Eq. 2 and is a consequence of the log-scale).

2.3 Synthetic experiment design

We apply GlaDS with the flux parameterizations in Table 2 to a synthetic ice-sheet margin domain with both synthetic and realistic temperature forcings. The synthetic domain and temperature forcing isolates differences between the models by reducing external controls on the drainage configuration, while the realistic temperature forcing allows us to assess differences in seasonal pressure patterns given plausible variations in surface melt rate that impact the development of efficient drainage in summer.

2.3.1 Domain and geometry

The model is applied to a 100 km × 25 km domain with ice thickness similar to the SHMIP experiment (de Fleurian and others, 2018) (Fig. 3a). The domain is adapted to coarsely represent the K-transect in western Greenland to ensure the surface melt forcing (Section 2.3.2) and geometry are consistent. The bed is flat with an elevation of 350 m, which approximates the ice-margin elevation near the K-transect (Smeets and others, 2018). The minimum ice-surface elevation is 390 m at the terminus (approximately equal to the elevation of the lowest K-transect station; van de Wal and others, 2005). The surface elevation is computed as

$$z_{\mathrm{s}} = 6\left(\sqrt{x + 5000} - \sqrt{5000}\right) + 390 \tag{5}$$

for x measured in metres from the terminus. The maximum surface elevation is 1909 m, which is near or above the modern-day ELA of >1700 m a.s.l. (Smeets and others, 2018).

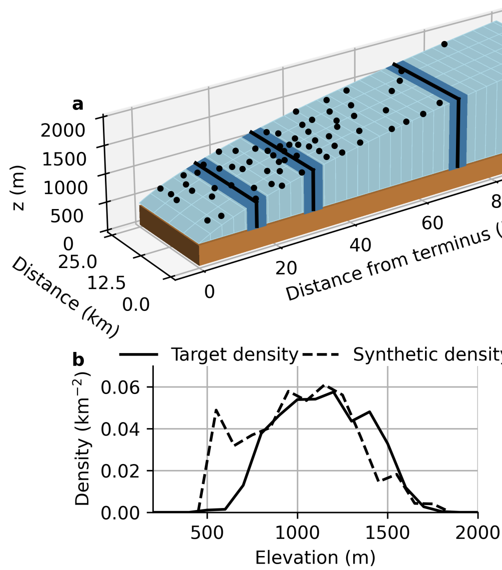

Fig. 3. Overview of synthetic model domain and moulin distribution. (a) Surface and bed elevation with moulins indicated by black circles. The bands at 15, 30, and 70 km indicate where model variables are aggregated in other figures. (b) Target moulin density (derived from Yang and Smith 2016) and density of randomly generated synthetic moulin design as a function of surface elevation.

2.3.2 Melt forcing

The subglacial model is forced with steady basal melt (0.01 m w.e. a^{-1}, Table 1) and seasonally varying surface melt. Since our focus is on seasonal evolution of subglacial drainage, we neglect diurnal variations in surface melt rate. We have found that seasonal water pressure patterns and the relative performance of the flux models (Table 2) are not sensitive to diurnal variations (Fig. S6). Spatially distributed surface melt rates are computed from a prescribed sea-level temperature $T_0(t)$ using a temperature-index model,

$$\dot{m}(z, t; \Gamma) = \max\left(0, f_{\mathrm{m}}\left(T_0(t) - \Gamma z\right)\right), \tag{6}$$

for melt factor f_{m}, temperature lapse rate Γ, and elevation above sea level z. The melt factor $f_{\mathrm{m}} = 0.01$ m w.e. a^{-1} °C^{-1} is taken from the SHMIP experiment (de Fleurian and others, 2018), and the temperature lapse rate $\Gamma = 0.005$°C m^{-1} is chosen to be consistent with summer lapse rates observed in west Greenland (Fausto and others, 2009).

GlaDS is forced with two sea-level temperature timeseries:

1. "Synthetic" forcing using a sea-level temperature parameterization adapted from the SHMIP experiment case D3 (de Fleurian and others, 2018):

$$T_0(t) = -a \cos\left(\frac{2\pi t}{T_{\text{year}}}\right) + b, \tag{7}$$

where constants a and b control the intensity and duration of surface melt, and T_{year} is the number of seconds in a year.

2. "KAN" forcing using daily mean air temperatures recorded at the PROMICE KAN_L weather station (How and others, 2022). We use temperatures from 2014, a representative year in terms of total volume and duration of surface melt over the 2009–2022 period (Fig. S1)

Prior to applying the above forcings, we forced the model with surface melt identical to that of the SHMIP experiment case D3. Modelled subglacial drainage for the turbulent 5/4 model (as used in the SHMIP experiment) recreates the published SHMIP outputs (Fig. S7) (de Fleurian and others, 2018).

The constants a and b for the synthetic forcing scenario presented here are computed to retain the same duration of positive sea-level temperatures as the SHMIP experiment and to result in the same total melt volume as the KAN scenario so that only the temporal variations in surface melt rate, and not the total melt volume, vary by scenario. We also tested the sensitivity to total melt volume by increasing the temperatures in the KAN timeseries to produce the same total melt volume as the original SHMIP case D3 (Fig. S8), but present the results for the observed melt volume since these results are expected to be more realistic.

2.3.3 Moulins

Surface meltwater drains into the subglacial system through discrete moulin locations. Supraglacial catchments are generated by randomly placing catchment centroids throughout the domain according to a space-filling maximin design (i.e., a design that maximize the minimum distance between moulins) and with an elevation-dependent density derived from supraglacial mapping (Yang and Smith, 2016) (Fig. S2). The moulin density is greatest at 1138 m a.s.l., and we assign a total of 68 supraglacial catchment centroids, computed from the product of the observation-derived density and the hypsometry of our domain.

Supraglacial catchments are generated by drawing a Voronoi diagram from the catchment centroids (i.e., assigning each node in the mesh to the catchment of the nearest centroid), and moulins are placed as the node with the lowest surface elevation within each catchment subject to the constraints: (1) the minimum distance between neighbouring moulins is 2.5 km, and (2) moulins can not be placed on boundary nodes or within 5 km of the terminus. Fig. S2 illustrates the moulin and catchment generation scheme in more detail.

Surface meltwater is accumulated within catchments and instantly routed into moulins. This scheme neglects the impact of supraglacial hydrology, which characteristically delays the diurnal peak and reduces the diurnal amplitude of surface inputs to moulins compared to the diurnal cycle of surface melt rate (e.g., Muthyala and others, 2022). This simplification is appropriate in our synthetic model setup considering the idealized nature of our experiments and since we are not attempting to resolve diurnal cycles in water pressures in response to diurnal variations in moulin inputs.

2.3.4 Boundary and initial conditions

The subglacial model is posed on an unstructured triangular mesh. We apply GlaDS on a mesh with 4156 nodes and a mean edge length of 883 m. This mesh resolution was chosen from mesh refinement tests as a suitable tradeoff between precision and computation time (Fig. S3). Boundary conditions consist of a zero-pressure boundary condition at the terminus ($x = 0$ km) and a zero-flux condition elsewhere.

GlaDS simulations involve a steady-state spin-up used as initial conditions for periodic runs. The spin-up is accomplished in three phases to ensure numerical stability: (1) 25 years with no surface inputs, starting with a uniform water depth equal to half the bed bump height and no subglacial channels (a sufficient duration for the model to evolve to an intermediate winter-like state that is independent of the uniform initial condition); (2) 25 years with a linear ramp-up of surface melt intensity; and (3) 50 years with constant melt rates to reach a final steady state (evaluated based on the rate-of-change of average water pressure). A steady state drainage configuration is typically reached well before the end of (3), but with implicit and adaptive timestepping the extra spin-up time is associated with negligible increases in runtime.

Periodic simulations are run for two years, and only results from the second year are analyzed. It would also be possible to begin seasonal simulations directly from the uniform initial condition, however this would require the transient simulations to be run for many melt seasons to reach a periodic state, so it is faster to approach the periodic state from an already channelized system, i.e., from the steady simulation.

3 RESULTS

3.1 Synthetic scenario

To illustrate the differences between modelled water pressure for the five flux parameterizations (Table 2), we first present modelled subglacial water pressure (normalized by overburden) and channel discharge for the synthetic forcing scenario (Fig. 4). The primary difference in modelled subglacial drainage is a result of the flux parameterization family (i.e., turbulent, laminar, and transition), with only minor differences related to α_s (i.e., between turbulent 5/4 and turbulent 3/2, and transition 5/4 and transition 3/2).

These model outputs confirm the well-known winter water pressure problem for the standard turbulent 5/4 model, which tends to produce unrealistically low winter and high summer water pressures (e.g., de Fleurian and others, 2018; Poinar and others, 2019; Ehrenfeucht and others, 2023). For this scenario, the turbulent models predict winter water pressures of 20% of overburden at 30 km with $\alpha_\mathrm{s} = 5/4$ and 30% with $\alpha_\mathrm{s} = 3/2$ (Table 3). These modelled winter water pressures are low compared to borehole observations close to overburden (e.g., winter water pressure higher than 95% of overburden 7 km from the ice margin (van de Wal and others, 2015); ∼80–100% of overburden 27 km from the ice margin (Wright and others, 2016)), even after accounting for the difference in pressure between connected and disconnected bed patches (e.g., Rada Giacaman and Schoof, 2023). The winter water pressure is improved for the laminar (57% of overburden at 30 km), transition 5/4 (57%), and transition 3/2 (57%) models relative to the turbulent models. Summer water pressure is broadly similar for all models, with the turbulent model predicting the highest pressure (turbulent 80% of overburden at 30 km; laminar 78%; transition 79–80%) (Table 3). The relative performance of the five models in Fig. 4 is the same as that obtained with surface melt forcing identical to the SHMIP experiment D3 (Fig. S7). The reduced melt volume in the synthetic scenario compared to the SHMIP experiment results in summer water pressure below overburden for all models.

The laminar and transition models predict a limited duration of elevated summer water pressure compared to the turbulent model (Fig. 4g-i; Table 3). Along with this seasonal pressure pattern, the laminar and transition models develop a more extensive channel network, with channels ($Q > 1$ m^3 s^{-1}) extending above 30 km, in contrast to channels being limited to the lowermost 15 km for the turbulent models. Peak channel discharge exceeds 100 m^3 s^{-1} with laminar and transition models but is below 50 m^3 s^{-1} for the turbulent models.

The differences in water pressure and drainage configuration between the flux parameterizations can be

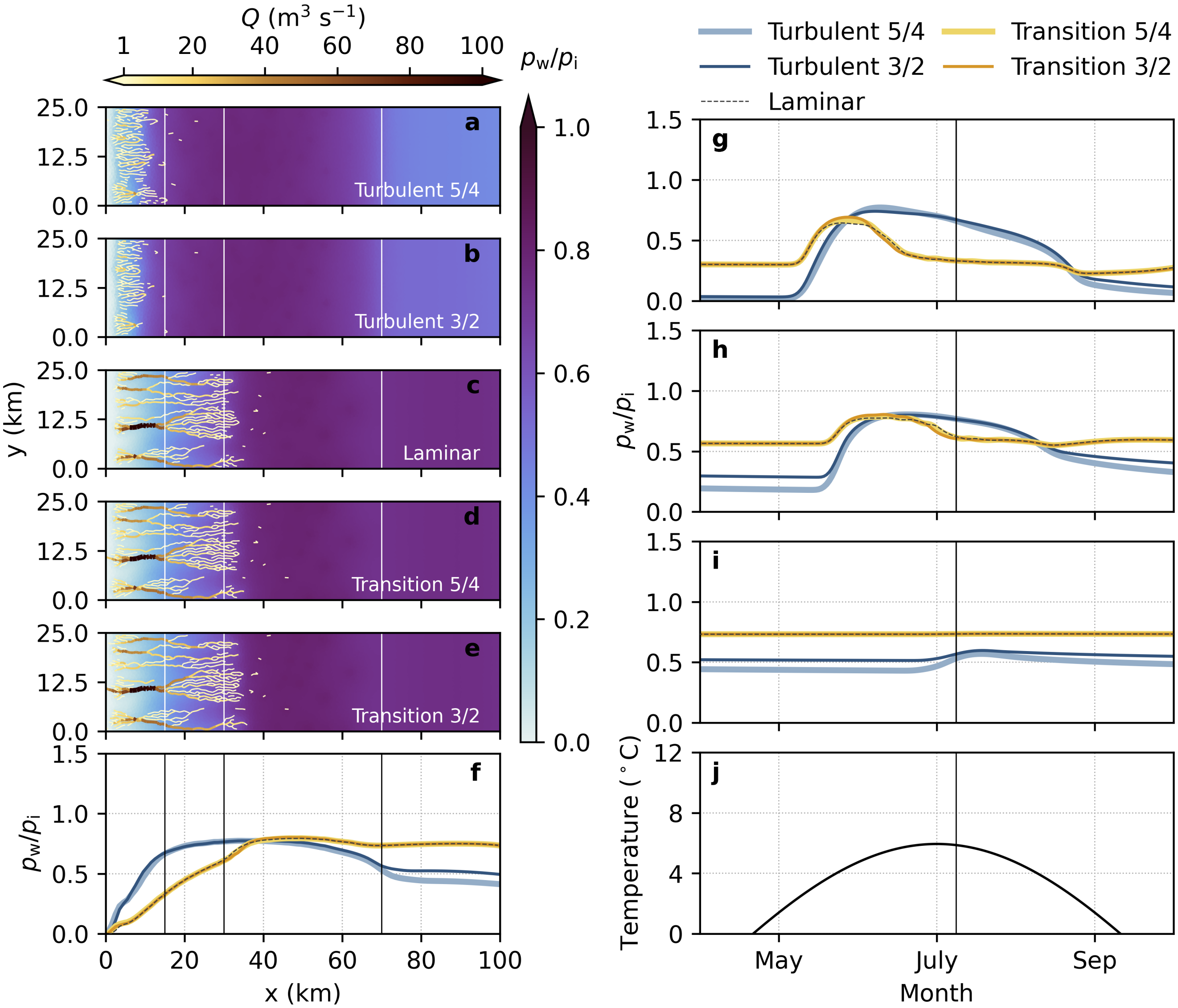

Fig. 4. Synthetic forcing scenario. Floatation fraction $\frac{p_w}{p_i}$ and channel discharge on 9 July (a-e) for turbulent 5/4 (a), turbulent 3/2 (b), laminar (c), transition 5/4 (d) and transition 3/2 (e) models, and width-averaged floatation fraction on 9 July (f). Width-averaged pressure in bands at $x = 15 \pm 2.5$ km (g), $x = 30 \pm 2.5$ km (h), and $x = 70 \pm 2.5$ km (i) and imposed air temperature at 390 m asl used to force the temperature-index model (j). The centre of bands used for (g–i) are indicated by vertical lines in (a–f), and the time of (a–f) is shown by vertical lines in (g–i).

Table 3. Water pressure normalized by overburden (i.e., floatation fraction) for synthetic and KAN temperature-forcing scenarios. Winter floatation fraction is computed as the average value within $x = 30 \pm 2.5$ km (Fig. 3) during the two months preceding the initial onset of surface melt. Summer floatation fraction is computed as the 95th-percentile width-averaged water pressure produced during the melt season within $x = 30 \pm 2.5$ km. The bracketed number beside summer floatation fractions for the KAN scenario indicates the number of days water pressure exceeded overburden. Water pressure does not exceed overburden in the Synthetic scenario.

		Floatation fraction (number of days above overburden)				
Scenario		Turbulent 5/4	Turbulent 3/2	Laminar	Transition 5/4	Transition 3/2
Synthetic	Winter	0.200	0.302	0.566	0.567	0.567
	Summer	0.804	0.799	0.775	0.786	0.800
KAN	Winter	0.237	0.334	0.577	0.577	0.577
	Summer	1.22 (22)	1.23 (23)	0.900 (1)	0.908 (3)	0.930 (2)

understood by considering the spatial and seasonal pattern in modelled Reynolds number, transmissivity, water depth, hydraulic potential, and conductivity (Fig. 5). The turbulence index (ωRe) highlights regions and times where the turbulent and laminar assumptions are inconsistent (Fig. 5a, b). The turbulent model assumes $\omega\mathrm{Re} \gg 1$ everywhere and for all times, so that the turbulent model is applied inappropriately above $x = 20$ km and outside of the peak summer season. On the other hand, the laminar model is inappropriate near $x = 20$ km, near the terminus, and during elevated summer water pressures.

Transmissivity, $T = \rho_w g \frac{q}{|\nabla\phi|}$, measures the discharge-per-unit-width associated with a specified potential gradient (Fig. 5c, d). It has similar spatial and seasonal patterns as the turbulence index ωRe. Transmissivity is higher for the turbulent models than the laminar and transition models during the summer, in part explaining the lack of channelization for the turbulent models (Fig. 4a–e).

The spatial and seasonal patterns in turbulence index ωRe can be decomposed into individual contributions from the water depth h (Fig. 5e,f) and potential gradient $|\nabla\phi|$ (Fig. 5g,h). Of the two components, the water depth h more strongly controls the turbulent index than the potential gradient. This is in line with the mathematically stronger dependence on h than the potential gradient, especially for the laminar and transition models.

The differences in seasonal water pressure variations between the turbulent, laminar, and transitions models are largely explained by variations in the effective turbulent conductivity, defined as $k_{\mathrm{eff}} = q/h^{5/4}|\nabla\phi|^{1/2}$ (Fig. 5i,j). By this definition, $k_{\mathrm{eff}} = k_{\mathrm{s}}$ for the turbulent 5/4 model, meaning that variations in the effective turbulent conductivity for other models allow them to be directly compared to the standard turbulent 5/4 model. For the remaining models, k_{eff} is a function of the water thickness and

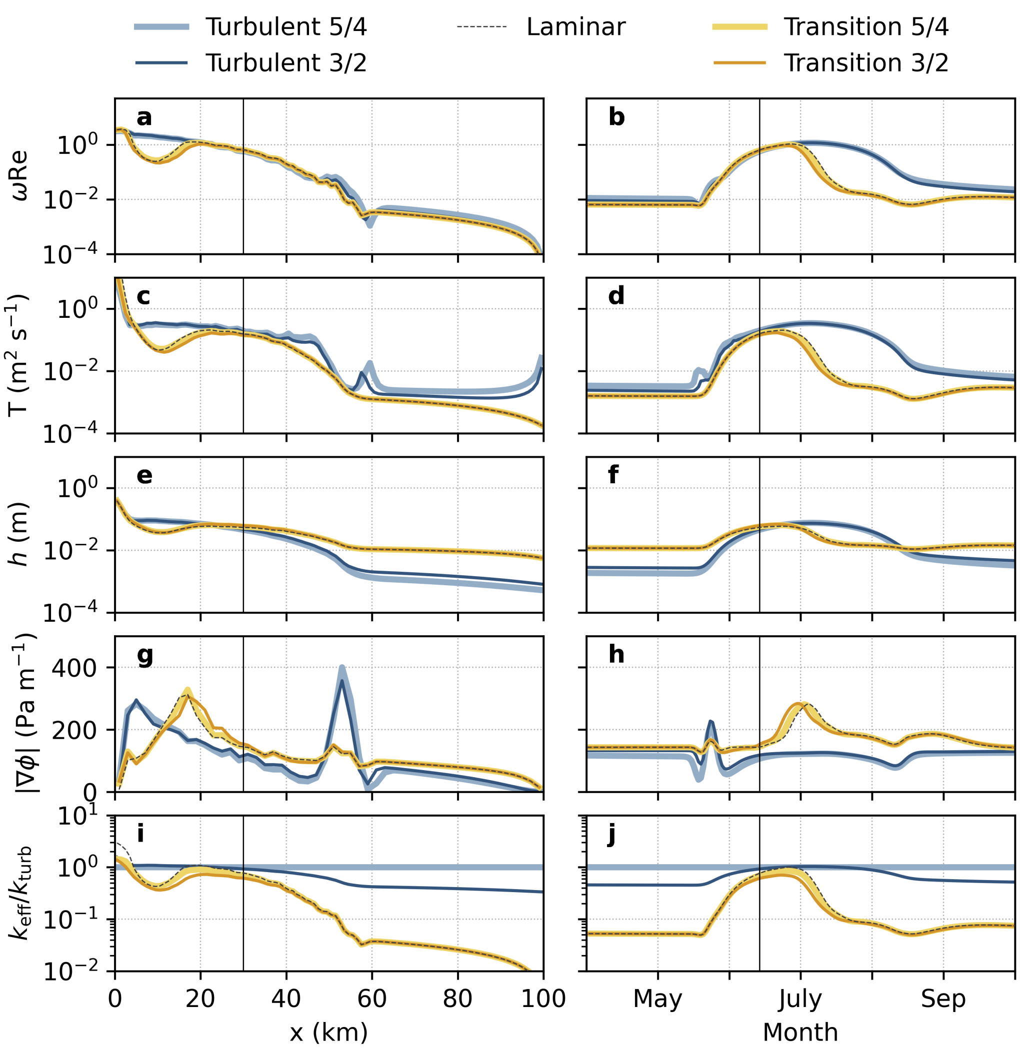

Fig. 5. Turbulence index $\omega\mathrm{Re}$ (log scale; a, b), transmissivity T (log scale; c, d), water depth h (log scale; e, f), potential gradient $|\nabla\phi|$ (linear scale; g, h), and effective turbulent conductivity (log scale; i, j) on 14 June (left column), and averaged for the band $x = 30 \pm 2.5$ km (right column).

potential gradient, with h again being the main driver based on its higher exponent. The k_{eff} for the laminar and transition models varies over two orders of magnitude in space (Fig. 5i) and more than one order of magnitude in time (Fig. 5j). The reduced effective conductivity for the laminar and transition models in winter explains the higher winter water pressure compared to the turbulent models, while the large seasonal changes in effective conductivity explain the reduced seasonal amplitude in water pressure compared to the turbulent models.

The spatial distribution of the Reynolds number just before peak melt (day 165, or 14 June) demonstrates the difference in channelization between the flux parameterizations (Fig. 6). The turbulent models have not transitioned to channel-dominated drainage, instead preferentially routing much larger volumes of meltwater through the distributed drainage system with higher associated Re. This lack of channelization arises from the higher effective conductivity compared to the other models (Fig. 5). The laminar model breaks down near the upstream limit of channelization as $\omega\mathrm{Re} > 1$, and again within the lowest part of the domain where boundary artifacts are present in all models. Since the laminar model does not properly represent distributed flow in the channel initialization zone, it may incorrectly predict the position or timing of the onset of channelized flow. However, the difference in the onset of channelization between the laminar and transition model is minor for the synthetic and KAN scenarios presented here and in tests including diurnal melt fluctuations (Fig. S6).

The results in Fig. 4 and 5 align with what is expected based on the Moody diagram (Fig. 7). Here the spread in the curves for the turbulent 5/4 (lighter blue) and transition 5/4 (lighter yellow) models is a result of the Re–f_{D} relationship depending on the hydraulic potential gradient, which varies in space and time. As shown by the effective turbulent conductivity (Fig. 5i,j), the turbulent models have significantly less flow resistance in winter compared to the laminar and transition models. The opposite slope of the curve for the turbulent 5/4 model further suggests a structural problem where flow resistance decreases with decreasing water supply (e.g., during winter), regardless of the chosen model parameters. This behaviour is not supported by the other models or the empirical friction factor curves. Of all the models, the transition 3/2 model (darker yellow) is closest to the empirical friction factor curves.

3.2 KAN scenario

The evolution of summer water pressure is sensitive to the temporal pattern of surface melt (Fig. 8). Despite identical total melt volumes between the synthetic and KAN temperature forcing scenarios, peak

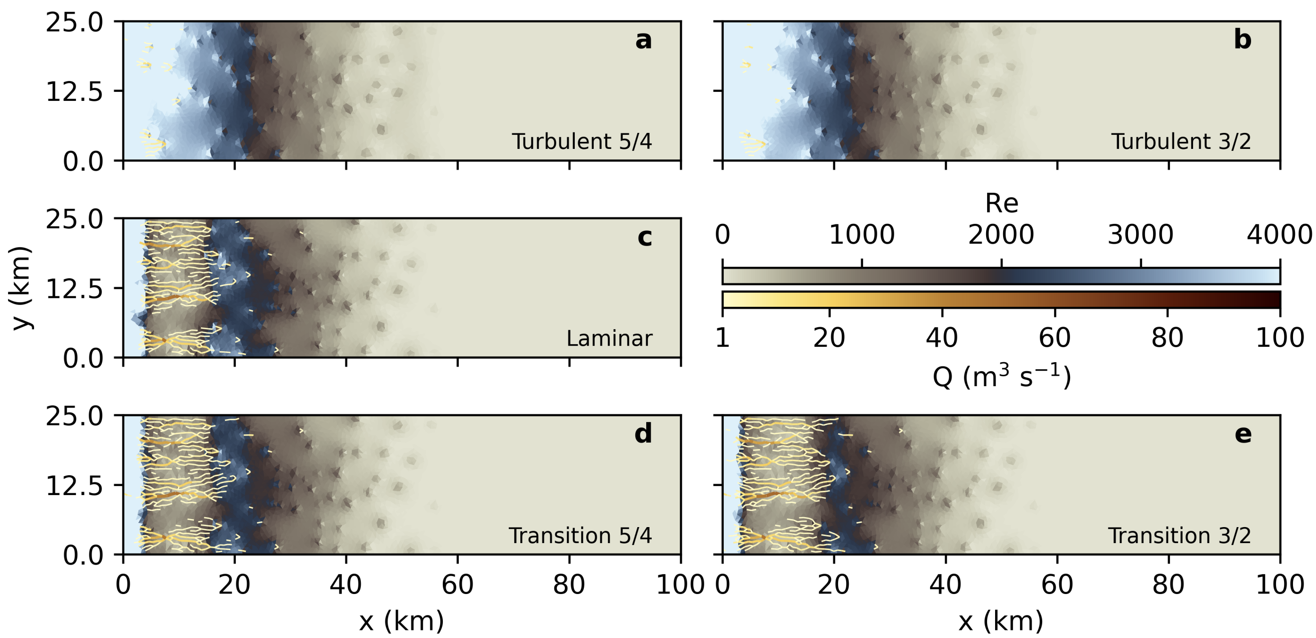

Fig. 6. Reynolds number and channel discharge for synthetic scenario on day 165 (14 June) for turbulent 5/4 (a), turbulent 3/2 (b), laminar (c), transition 5/4 (d), and transition 3/2 (e) models.

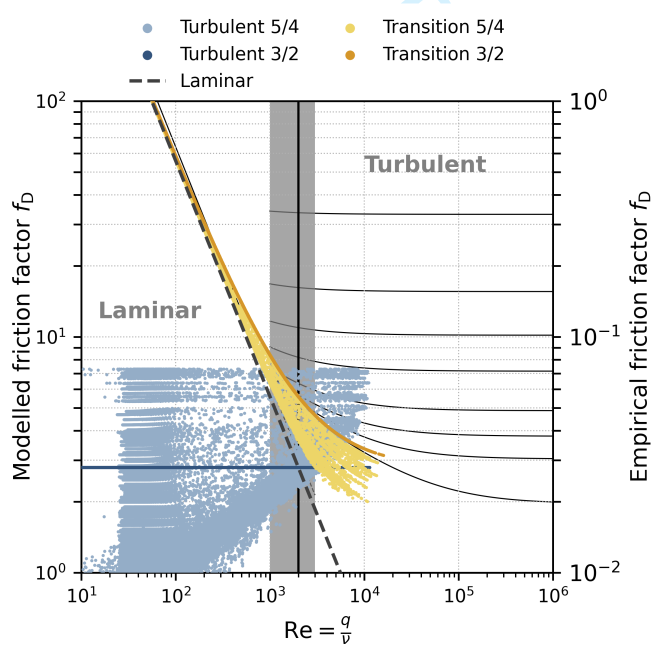

Fig. 7. Moody diagram computed from model outputs in the synthetic scenario for the five flux parameterizations (Table 2). The turbulent 3/2 model appears as a horizontal line since its friction factor is independent of Re and $\nabla\phi$. The transition Reynolds number is shown as the solid black line at $\mathrm{Re} = 2000$. For reference, the classical pipe-flow Moody diagram from Fig. 1 is shown in the background (black, right axis).

summer water pressures are higher with KAN temperature forcing (Table 3, S1).

The turbulent 5/4 and turbulent 3/2 models once again predict low winter water pressure (24% and 33% of overburden at $x = 30$ km) compared to the laminar (58%) and transition (58%) models (Table 3). The turbulent models predict water pressure well above the winter baseline for the entirety of the melt season, whereas the laminar and transition models predict late-summer water pressure below the winter baseline. Peak summer water pressures at 30 km are highest for the turbulent 5/4 (122% with 22 days above floatation) and turbulent 3/2 (123% with 23 days above floatation) models, with representative summer presure below overburden for the laminar (90% with 1 day above floatation) and transition (91% to 93% with 2–3 days above floatation) models. Pressures above overburden occur during four distinct melt events at 30 km with the turbulent models, and only during the first melt event with laminar and transition models. These peak summer pressures are higher than in the synthetic scenario (<80%) due to greater variability in the KAN temperatures.

The controls on differences in water pressure between the flux parameterizations are the same as for the synthetic scenario. The opposing sensitivity of the friction factor (i.e., flow resistance) to the Reynolds number (i.e., flow intensity) for the turbulent models compared to the laminar and transition models (Fig. 7) results in significantly lower winter water pressure and a larger variation between winter and summer water pressure for the turbulent models.

To ensure the qualitative differences observed between the synthetic and KAN forcings are not a function of seasonal melt volume, we re-ran the KAN simulations with the original SHMIP D3 (larger) seasonal melt volume. To do this, we increased the temperatures in the KAN timeseries by 2.43°C and adjusted the lapse rate to $\Gamma = -0.0075$°C m^{-1} to produce the desired seasonal melt volume. The qualitative differences related to the flux parameterizations are robust with respect to this change in total melt volume, however the modelled water pressure is unrealistically high during melt events, reaching almost 300% of overburden for the turbulent models (Fig. S8).

3.3 Parameter sensitivity

The results for the synthetic (Fig. 4) and KAN (Fig. 8) scenarios represent a single set of parameter values. To assess whether the differences between the five flux parameterizations are a function of parameter choice, we perform a simple sensitivity test where parameters are specifically chosen to maximize the performance of the turbulent models in capturing high winter water pressure, late-summer pressure below

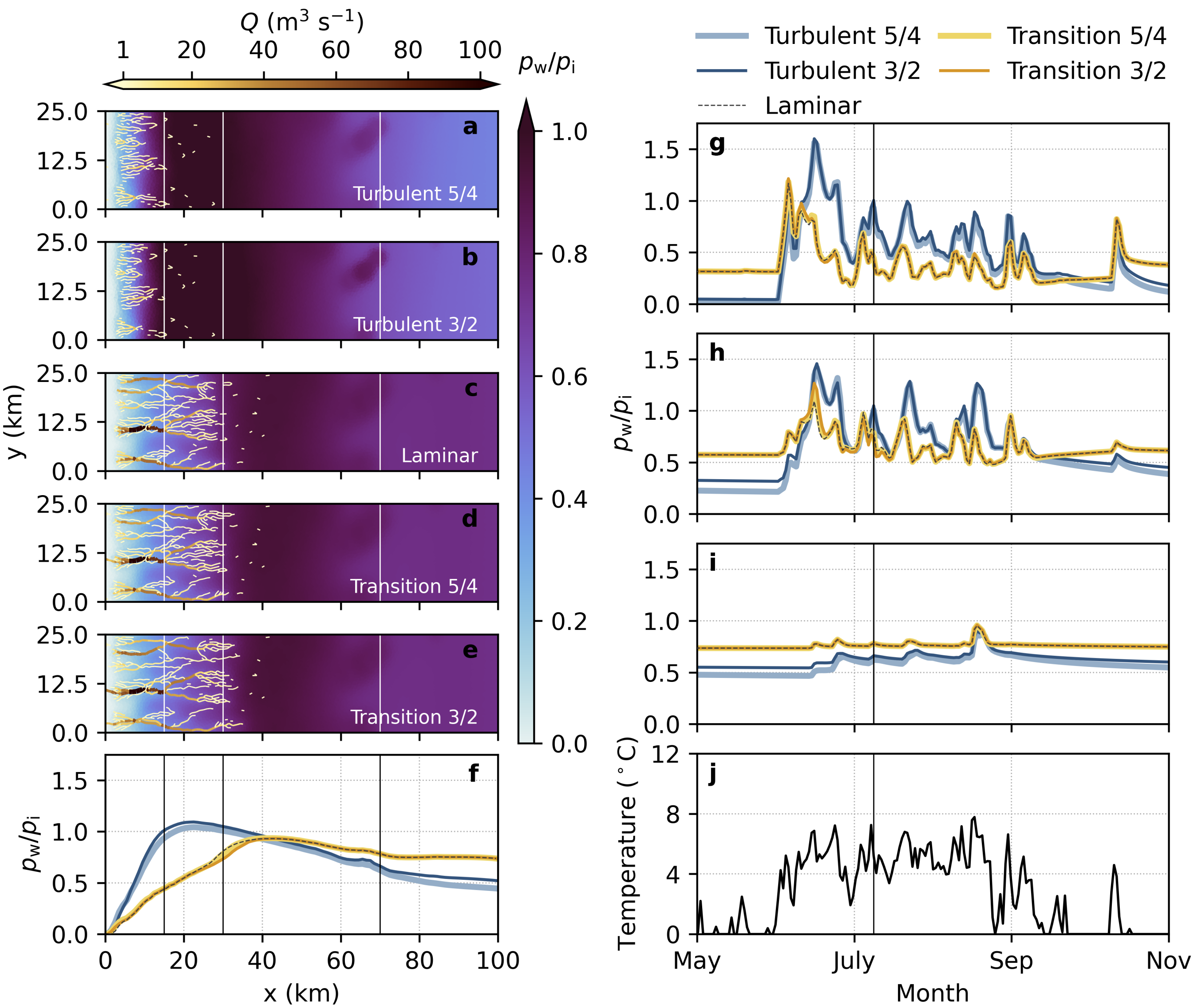

Fig. 8. KAN forcing scenario. Floatation fraction $\frac{p_w}{p_i}$ and channel discharge on 2 August (a-e) for turbulent 5/4 (a), turbulent 3/2 (b), laminar (c), transition 5/4 (d) and transition 3/2 (e) models, and width-averaged floatation fraction on 2 August (f). Width-averaged pressure in bands at $x = 15 \pm 2.5$ km (g), $x = 30 \pm 2.5$ km (h), and $x = 70 \pm 2.5$ km (i) and imposed air temperature at 390 m asl used to drive the temperature-index model (black curve, right axis g–i). The centre of bands used for (g–i) are indicated by vertical lines in (a–f), and the time of (a–f) is shown by vertical lines in (g–i).

winter baseline, spring pressure maximum near ice overburden and Re consistent with a priori assumptions.

Despite these efforts, the optimized turbulent 5/4 and turbulent 3/2 models still fall short of the desired behaviour seen by the reference laminar and transition models (Fig. S9). However, the modelled drainage configuration has become fully inconsistent with the turbulent flow assumption. The Reynolds number for the turbulent models is uniformly below ∼1000 throughout the melt season (Fig. S10), well below the prescribed transition threshold (2000) and the empirical transition point (2000–3000; Fig. 1). The Reynolds number therefore suggests that the partial improvements in modelled water pressure are a result of forcing the turbulent model outside its domain of applicability. The persistent shortcomings of the turbulent model suggest that any remaining failures are structural rather than a consequence of a particular choice of parameters.

4 DISCUSSION

4.1 Distributed water flux parameterizations

We have presented modelled subglacial drainage configurations for five flux parameterizations (Table 2). With both synthetic and KAN surface melt forcing, laminar and transition models show desirable behaviour compared to the turbulent models. The laminar and transition models result in higher winter water pressure, late-summer water pressure minima below the winter baseline, and more realistic pressure variations between winter and the spring pressure maximum. These desirable features are more clear in the KAN scenario (Fig. 8), since the smooth melt forcing in the synthetic scenario results in muted seasonal pressure variations (Fig. 4). Given the consistently lower performance of the turbulent model, even with parameters selected to maximize its performance (Fig. S9), these findings do not appear to be a consequence of the particular parameter values used throughout. Considering the similar performance of the laminar and transition models, the advantage of the transition model is in its conceptual ability to interpolate between laminar and turbulent end-members to represent flows across the complete range of modelled Reynolds number (Fig. 6).

The laminar model is less problematic than the turbulent model, and only minimally deviates from the transition model, but it has difficulty near the ice-sheet margin compared to other models. Where the ice is thin and therefore the rate of creep closure of the cavity roof is slow, the height of subglacial cavities approaches the bed bump height and the Reynolds number becomes large relative to the specified transition threshold (Fig. 6). In this regime, the laminar model underestimates flow resistance (Fig. 7), resulting in flow nearly completely transitioning from channelized to distributed within the final few mesh elements near the margin (Fig. 6). This occurs to some degree for all models, and is reduced when parameters are adjusted to increase the preference for channelization, but the problem is most pronounced for the laminar model. Given observations of meltwater emerging from beneath the ice sheet in discrete proglacial streams (e.g., Chandler and others, 2013; Smith and others, 2015) and sediment plumes (e.g., Chu and others, 2009), we expect subglacial channels should reach the terminus.

Unrealistic modelled winter water pressure has previously been addressed using the turbulent 5/4 model by prescribing the sheet conductivity k_s as a linear function of surface melt rates to allow for reduced conductivity during winter and increased conductivity during summer (Downs and others, 2018). The result of this conductivity parameterization is a similar seasonal pattern of turbulent conductivity as reproduced by the laminar and transition models (Fig. 5j). The major difference between the laminar and transition models and the Downs and others (2018) parameterization is the magnitude of variation. Downs and others (2018) prescribe the conductivity to vary on the order of $\mathcal{O}(10^4)$ in time but remain constant in space, whereas we have a variation of order $\mathcal{O}(10^1)$ in time, and order $\mathcal{O}(10^2)$ in space. These variations in our model results have not been prescribed, but emerge naturally as a result of the flux parameterizations.

Seasonal pressure variations have been shown to depend on the evolving connectivity of distributed drainage elements, where low winter water pressure in connected bed regions may by compensated for by high pressure within disconnected bed regions (e.g., Andrews and others, 2014; Hoffman and others, 2016; Rada Giacaman and Schoof, 2023). By comparing a coupled hydrology–dynamics model to sliding speed, subglacial discharge, and ice thickness data from Argentière Glacier, Gilbert and others (2022) found a turbulent flow exponent $\alpha_s \geq 5$ provided the best fit to observed velocities. The high value for the turbulent flow exponent was interpreted as possibly representing a switch in bed connectivity as a function of the water thickness h (e.g., Flowers, 2000; Helanow and others, 2021). In other words, Gilbert and others (2022) suggest that some of the net effects of changing bed connectivity can be included by increasing the sheet-flow exponent α_s. In this context, some of the poor performance of the turbulent model can be attributed to its failure to represent decreased hydraulic connectivity (i.e., taking f_D^{-1} as a proxy for connectivity) in winter. Based on these considerations, the possibility that $\alpha_s > 3$ for sub-turbulent flows, in particular for the transition model, should be investigated if further data suggest that $\alpha_s > 3$ can reproduce key features related to changes in bed connectivity.

The advantage of the laminar and transition models over the turbulent model is therefore in the improved seasonal water pressure patterns. The advantage of the transition models over the laminar model is more subtle and has to do with the internal inconsistencies of the laminar model (e.g., Fig. 5, 6) and the timing of channelization. For example, the laminar model does not produce channels reaching the terminus, while the transition models develops channels reaching the terminus between 14 June (Fig. 6) and 9 July (Fig. 4, 8). While the large cavities and reduced channelization obtained with all models near the margin is unrealistic, the laminar model predicts slower and reduced channelization within this region relative to the transition models due to its overestimation of sheet flux at high Re.

These advantages in the laminar and transition models over the turbulent model come with minimal costs in terms of the difficulty running the model and in the computational burden. Running the laminar model only requires a trivial change in parameters (α_s, β_s, and appropriately scaling the conductivity k_s in Eq. (1)). Running the transition model requires a simple modification of the model source code to replace Eq. (1) with Eq. (2). The laminar and transition models need between 57% and 200% of the computation time required for the turbulent 5/4 model, although the top end of this range may be able to be reduced through optimizing the adaptive timestepping (Table S2).

4.2 Turbulent flow exponent

The turbulent flow exponent (α_s in Eqs. (1) and (2), Table 1) has a secondary impact on modelled water pressure and drainage configuration relative to the primary control of the form of the flux parameterization. However, winter water pressure for the turbulent model is sensitive to the value of α_s, with the turbulent 3/2 model predicting higher (slightly more realistic) winter water pressure (e.g., Fig. 8h). Sensitivity is very low for the transition model, since the turbulent exponent α_s only applies in fully turbulent $\omega\mathrm{Re} \gg 1$ limit, which is rarely reached in our model configuration (Fig. 7).

Given that the fully turbulent limit is not reached in our model outputs (Fig. 7), the choice of α_s for the turbulent and transition models can not be assigned strictly from Darcy–Weisbach pipe flow theory. However, the upwards slope of the envelope of modelled friction factors for the turbulent 5/4 model in Fig. 7 is inconsistent with the other flux models and with empirical friction factor curves, suggesting that $\alpha_\mathrm{s} = 3/2$ is a more reasonable choice than $\alpha_\mathrm{s} = 5/4$.

Our model outputs and theoretical considerations suggest that $\alpha_\mathrm{s} = 3/2$ yields marginally more realistic outputs than $\alpha_\mathrm{s} = 5/4$ (i.e., ∼10% higher winter water pressure for comparable parameter values). For modelling studies that take the turbulent flow assumption, we recommend α_s be treated as an uncertain parameter and tuned where possible (e.g., Gilbert and others, 2022) rather than prescribed as $\alpha_\mathrm{s} = 5/4$ based on precedent. Given the minimal sensitivity for the transition model, and since the turbulent exponent α_s is only applied in the transition model in the true turbulent limit ($\omega\mathrm{Re} \gg 1$), it should be appropriate to use the transition 3/2 model, instead of transition 5/4, by default.

4.3 Choosing an appropriate flux parameterization

Considering the discussion of both the form (Section 4.1) and turbulent exponent (Section 4.2) of the distributed flux parameterization, we recommend the following:

1. Use the transition 3/2 model by default based on its theoretical (i.e., unlimited Re range of applicability; Fig 7) and practical (i.e., desirable features in modelled water pressure; Fig. 8) attributes.

2. If only aggregate model outputs (e.g., spatio-temporally averaged basal effective pressure) are important, the laminar model may be appropriate as an approximation of the transition model. In this case, it should be verified that the modelled Reynolds number does not reach the turbulent regime, since the model is physically inconsistent and may overestimate sheet flux with $\omega\mathrm{Re} > 1$.

3. Avoid the turbulent model for seasonally varying subglacial drainage simulations, unless theoretical (i.e., modelled Reynolds number) and/or practical (i.e., demonstrated sensitivity of quantities of interest to the flux model) reasons are discovered that make its performance superior to the transition model. In this case, the turbulent 3/2 model is recommended over the turbulent 5/4 model, but sensitivity of any quantities of interest to the value of α_s should be assessed.

4.4 Study limitations

4.4.1 Model geometry and domain

There are a number of limitations related to the idealized model setup utilized here. We have presented results for a flat bed, which is not broadly representative of topography beneath Greenlandic outlet glaciers (e.g., Morlighem and others, 2017). To address this, we additionally tested the sensitivity of model outputs to different realizations of bed topography, including a bed with a ∼6 km-wide and 350 m-deep trough along the centre of the domain, and U-shaped bed topography (Fig. S12). These tests show no difference in the relative performance of each model since topography has a similar influence on water pressure for all flux parameterizations (Fig. S13, S14). These tests suggest that the performance of the parameterizations are not sensitive to the choice of synthetic bed topography.

4.4.2 Surface meltwater forcing

Both the synthetic and KAN surface melt forcings used here are simplified relative to realistic surface melt rates. The KAN forcing scenario, derived from daily mean temperatures recorded at the KAN_L AWS (How and others, 2022) and a simple temperature-index model, elicits a more realistic water pressure response than the unrealistic synthetic scenario. For the KAN forcing, we have used a single sample of temperature forcing measured at the KAN_L PROMICE station. This timeseries was chosen to be representative in terms of the total melt volume and melt season duration, however different temperature timeseries will result in different modelled water pressures. Given the consistency of the differences between the flux parameterizations between the synthetic (Fig. 4) and KAN scenarios (Fig. 8), it is unlikely the performance differences of the flux parameterizations are a function of the choice of temperature timeseries.

Since we are focused on subglacial water pressure on seasonal timescales, we have chosen to omit diurnal variations in forcing the subglacial drainage model. We have also ignored supraglacial (e.g., Poinar and Andrews, 2021; Hill and Dow, 2021) and englacial (e.g., Andrews and others, 2022) hydrologic processes that impact the diurnal evolution of water pressure (e.g., Andrews and others, 2018). Neglecting diurnal oscillations has previously been shown to have only a limited impact on the seasonal development of the subglacial drainage system (e.g., Werder and others, 2013), and experiments with prescribed diurnal forcing show a minimal impact (Fig. S6).

4.4.3 Reynolds number and transition parameter

The partitioning between laminar and turbulent flow (Fig. 5) has been based on the Reynolds number computed using the distributed flux q, which represents the average flux through many subglacial cavities within each model element. It is therefore not exactly clear how representative this bulk-averaged Re metric is of flow through physical subglacial drainage elements comprising the 'distributed water sheet' as represented in models. The problem of determining a representative Reynolds number is shared by models of non-Darcy porous flow (e.g., Ward, 1964; Bear, 1972; Venkataraman and Rao, 1998). In this context, the problem can be partially addressed by direct numerical simulation of flow through a particular medium (e.g., Wood and others, 2020). Given the uncertainty in the exact form of subglacial drainage elements, this is not a question that can be answered within the framework of current subglacial hydrology models, but it is important to consider when assigning the transition parameter ω, since the Reynolds number cannot be interpreted as precisely as for simple flows. We have assumed that the transition from laminar to turbulent flow occurs at $\mathrm{Re} \approx 2000$, but it remains to be shown what transition threshold yields the best agreement with velocity or subglacial water pressure data in more realistic model settings.

5 CONCLUSIONS

Subglacial drainage models are key to understanding the relationship between surface and basal melt, basal motion, and ultimately grounded-ice contributions to sea level (e.g., King and others, 2020). However, these models have important shortcomings when applied to ice-sheet-scale domains with seasonally varying melt forcing. Subglacial models (1) underpredict winter water pressures, (2) fail to capture the late-summer pressure minimum (3) predict unrealistically large spring pressure peaks, and (4) require a priori assumptions about distributed flow being fully laminar or turbulent. We have demonstrated that these four problems can be measurably addressed by modifying the parameterization controlling water flux in the distributed (linked-cavity) drainage system while maintaining purely turbulent flow within subglacial channels.

We have tested five flux parameterizations (Table 2), including the standard turbulent model (e.g., Schoof and others, 2012; Werder and others, 2013), the fully laminar model (e.g., Hewitt, 2013; Gagliardini and Werder, 2018; Cook and others, 2022), and a parameterization that transitions between laminar and turbulent flow based on the local Reynolds number, for two values of the turbulent flow exponent where appropriate ($\alpha_\mathrm{s} = 5/4, 3/2$). The flux parameterizations are tested within the GlaDS model (Werder and others, 2013) using synthetic and realistic seasonally varying air temperature forcing on a synthetic ice-sheet margin domain.

Laminar and transition models outperform turbulent models on all identified criteria. Winter water pressure is increased by ~25–35% of overburden across the domain for the laminar and transition models for comparable parameter values. At the same time, the duration of pressures exceeding overburden is reduced from 22–23 days with the turbulent models to at most 3 days with laminar and transition models. In all scenarios, the turbulent model predicts summer water pressure well above the winter baseline pressure, whereas the the laminar and transition models produce late-summer water pressures below the winter baseline in the KAN forcing scenario. Fundamentally, the turbulent and laminar models are inconsistent with their underlying assumptions when extrapolated to Reynolds numbers inappropriate for their respective assumptions (e.g., Fig 7).

We suggest using the transition ($\alpha_s = 3/2$) model where possible based on its desirable features and physical consistency in representing flows with a complete range of Reynolds numbers. The laminar model produces similar results for seasonal-scale simulations, but suffers from conceptual inconsistencies. The turbulent model should be used with caution and an appreciation of its structural limitations.

Our results suggests that the parameterization of sheet-flow is crucial for modelling realistic seasonal water-pressure variations. It is an open question how this simple modification might impact the results of coupled hydrology–dynamics modelling (e.g., Gagliardini and Werder, 2018; Cook and others, 2022; Ehrenfeucht and others, 2023). Future work should explore the extent to which models with a sheet-flow exponent $\alpha_s > 3$ can represent some of the impacts of hydraulically disconnected drainage elements (e.g., Gilbert and others, 2022), and in what flow regimes this is appropriate.

CODE AND DATA AVAILABILITY

Code to run GlaDS and analysis scripts are available online at `https://github.com/timghill/glads-laminar-turbuler` GlaDS-Matlab code is available by request to Mauro Werder. PROMICE AWS data is available online at `https://doi.org/10.22008/FK2/IW73UU` (How and others, 2022).

ACKNOWLEDGEMENTS

TH was supported by the Natural Sciences and Engineering Council of Canada (NSERC) Canada Graduate Scholarhip program. GF received support from the NSERC Discovery Grants program. This research was enabled in part by support provided by WestDRI (`https://training.westdri.ca`) and the Digital Research Alliance of Canada (`https://alliancecan.ca`).

AUTHOR CONTRIBUTIONS

TH, GF, DB, and MH conceived of the idea of modifying the subglacial sheet-flow parameterization and designed the experiments. TH implemented the transition parameterization within GlaDS and ran the model, including analyzing and visualizing model outputs. TH, GF, and MH interpreted the model results with input from MW. TH prepared the manuscript with contributions from GF, MH, and MW.

REFERENCES

Andrews LC, Catania GA, Hoffman MJ, Gulley JD, Lüthi MP, Ryser C, Hawley RL and Neumann TA (2014) Direct observations of evolving subglacial drainage beneath the Greenland Ice Sheet. *Nature*, **514**(7520), 80–83 (doi: 10.1038/nature13796)

Andrews LC, Hoffman MJ, Neumann TA, Catania GA, Lüthi MP, Hawley RL, Schild KM, Ryser C and Morriss BF (2018) Seasonal evolution of the subglacial hydrologic system modified by supraglacial lake drainage in western Greenland. *Journal of Geophysical Research: Earth Surface*, **123**(6), 1479–1496 (doi: 10.1029/2017JF004585)

Andrews LC, Poinar K and Trunz C (2022) Controls on Greenland moulin geometry and evolution from the Moulin Shape model. *The Cryosphere*, **16**(6), 2421–2448 (doi: 10.5194/tc-16-2421-2022)

Banwell A, Hewitt I, Willis I and Arnold N (2016) Moulin density controls drainage development beneath the Greenland ice sheet. *Journal of Geophysical Research: Earth Surface*, **121**(12), 2248–2269 (doi: 10.1002/2015JF003801)

Bear J (1972) *Dynamics of fluids in porous media*. American Elsevier Publishing Company, ISBN 9780486131801

Brinkerhoff D, Aschwanden A and Fahnestock M (2021) Constraining subglacial processes from surface velocity observations using surrogate-based Bayesian inference. *Journal of Glaciology*, **67**(263), 385–403 (doi: 10.1017/jog.2020.112)

Bueler E and van Pelt W (2015) Mass-conserving subglacial hydrology in the Parallel Ice Sheet Model version 0.6. *Geoscientific Model Development*, **8**(6), 1613–1635 (doi: 10.5194/gmd-8-1613-2015)

Chandler DM, Wadham JL, Lis GP, Cowton T, Sole A, Bartholomew I, Telling J, Nienow P, Bagshaw EB, Mair D and others (2013) Evolution of the subglacial drainage system beneath the Greenland Ice Sheet revealed by tracers. *Nature Geoscience*, **6**(3), 195–198 (doi: 10.1038/ngeo1737)

Chu VW, Smith LC, Rennermalm AK, Forster RR, Box JE and Reeh N (2009) Sediment plume response to surface melting and supraglacial lake drainages on the Greenland ice sheet. *Journal of Glaciology*, **55**(194), 1072–1082 (doi: 10.3189/002214309790794904)

Colebrook CF and White CM (1937) Experiments with fluid friction in roughened pipes. *Proceedings of the Royal Society of London. Series A-Mathematical and Physical Sciences*, **161**(906), 367–381 (doi: 10.1098/rspa.1937.0150)

Cook SJ, Christoffersen P, Todd J, Slater D and Chauché N (2020) Coupled modelling of subglacial hydrology and calving-front melting at Store Glacier, West Greenland. *The Cryosphere*, **14**(3), 905–924 (doi: 10.5194/tc-14-905-2020)

Cook SJ, Christoffersen P and Todd J (2022) A fully-coupled 3D model of a large Greenlandic outlet glacier with evolving subglacial hydrology, frontal plume melting and calving. *Journal of Glaciology*, **68**(269), 486–502 (doi: 10.1017/jog.2021.109)

Creyts TT and Schoof CG (2009) Drainage through subglacial water sheets. *Journal of Geophysical Research: Earth Surface*, **114**(F4) (doi: 10.1029/2008JF001215)

Cuffey KM and Paterson WSB (2010) *The Physics of Glaciers*. Elsevier, Butterworth-Heineman, Oxford, 4 edition

Davison BJ, Sole AJ, Cowton TR, Lea JM, Slater DA, Fahrner D and Nienow PW (2020) Subglacial drainage evolution modulates seasonal ice flow variability of three tidewater glaciers in southwest Greenland. *Journal of Geophysical Research: Earth Surface*, **125**(9), e2019JF005492 (doi: 10.1029/2019JF005492)

de Fleurian B, Gagliardini O, Zwinger T, Durand G, Le Meur E, Mair D and Råback P (2014) A double continuum hydrological model for glacier applications. *The Cryosphere*, **8**(1), 137–153 (doi: 10.5194/tc-8-137-2014)

de Fleurian B, Werder MA, Beyer S, Brinkerhoff DJ, Delaney I, Dow CF, Downs J, Gagliardini O, Hoffman MJ, Hooke RL and others (2018) SHMIP the subglacial hydrology model intercomparison project. *Journal of Glaciology*, **64**(248), 897–916 (doi: 10.1017/jog.2018.78)

Dow CF, Kulessa B, Rutt IC, Tsai VC, Pimentel S, Doyle SH, van As D, Lindbäck K, Pettersson R, Jones GA and Hubbard A (2015) Modeling of subglacial hydrological development following rapid supraglacial lake drainage. *Journal of Geophysical Research: Earth Surface*, **120**(6), 1127–1147 (doi: 10.1002/2014JF003333)

Dow CF, McCormack FS, Young DA, Greenbaum JS, Roberts JL and Blankenship DD (2020) Totten Glacier subglacial hydrology determined from geophysics and modeling. *Earth and Planetary Science Letters*, **531**, 115961 (doi: 10.1016/j.epsl.2019.115961)

Dow CF, Ross N, Jeofry H, Siu K and Siegert MJ (2022) Antarctic basal environment shaped by high-pressure flow through a subglacial river system. *Nature Geoscience*, 1–7 (doi: 10.1038/s41561-022-01059-1)

Downs JZ, Johnson JV, Harper JT, Meierbachtol T and Werder MA (2018) Dynamic hydraulic conductivity reconciles mismatch between modeled and observed winter subglacial water pressure. *Journal of Geophysical Research: Earth Surface*, **123**(4), 818–836 (doi: 10.1002/2017JF004522)

Ehrenfeucht S, Morlighem M, Rignot E, Dow CF and Mouginot J (2023) Seasonal acceleration of Petermann glacier, Greenland, from changes in subglacial hydrology. *Geophysical Research Letters*, **50**(1), e2022GL098009 (doi: 10.1029/2022GL098009)

Fausto RS, Ahlstrøm AP, Van As D, Bøggild CE and Johnsen SJ (2009) A new present-day temperature parameterization for Greenland. *Journal of Glaciology*, **55**(189), 95–105 (doi: 10.3189/002214309788608985)

Felden AM, Martin DF and Ng EG (2023) SUHMO: an adaptive mesh refinement SUbglacial Hydrology MOdel v1. 0. *Geoscientific Model Development*, **16**(1), 407–425 (doi: 10.5194/gmd-16-407-2023)

Flowers GE (2000) *A multicomponent coupled model of glacier hydrology*. Ph.D. thesis, University of British Columbia (doi: 10.14288/1.0053158)

Flowers GE (2015) Modelling water flow under glaciers and ice sheets. *Proceedings of the Royal Society A: Mathematical, Physical and Engineering Sciences*, **471**(2176), 20140907 (doi: 10.1098/rspa.2014.0907)

Flowers GE and Clarke GKC (2002) A multicomponent coupled model of glacier hydrology 1. Theory and synthetic examples. *Journal of Geophysical Research: Solid Earth*, **107**(B11), ECV–9 (doi: 10.1029/2001JB001122)

Gagliardini O and Werder MA (2018) Influence of increasing surface melt over decadal timescales on land-terminating Greenland-type outlet glaciers. *Journal of Glaciology*, **64**(247), 700–710 (doi: 10.1017/jog.2018.59)

Gilbert A, Gimbert F, Thøgersen K, Schuler TV and Kääb A (2022) A consistent framework for coupling basal friction with subglacial hydrology on hard-bedded glaciers. *Geophysical Research Letters*, **49**(13), e2021GL097507 (doi: 10.1029/2021GL097507)

Hager AO, Hoffman MJ, Price SF and Schroeder DM (2022) Persistent, extensive channelized drainage modeled beneath Thwaites Glacier, West Antarctica. *The Cryosphere*, **16**(9), 3575–3599 (doi: 10.5194/tc-16-3575-2022)

Helanow C, Iverson NR, Woodard JB and Zoet LK (2021) A slip law for hard-bedded glaciers derived from observed bed topography. *Science Advances*, **7**(20), eabe7798 (doi: 10.1126/sciadv.abe7798)

Hewitt IJ (2013) Seasonal changes in ice sheet motion due to melt water lubrication. *Earth and Planetary Science Letters*, **371**, 16–25 (doi: 10.1016/j.epsl.2013.04.022)

Hewitt IJ, Schoof C and Werder MA (2012) Flotation and free surface flow in a model for subglacial drainage. Part 2. Channel flow. *Journal of Fluid Mechanics*, **702**, 157–187 (doi: 10.1017/jfm.2012.166)

Hill T and Dow CF (2021) Modeling the dynamics of supraglacial rivers and distributed meltwater flow with the Subaerial Drainage System (SaDS) model. *Journal of Geophysical Research: Earth Surface*, **126**(12), e2021JF006309 (doi: 10.1029/2021JF006309)

Hoffman MJ, Andrews LC, Price SF, Catania GA, Neumann TA, Lüthi MP, Gulley J, Ryser C, Hawley RL and Morriss B (2016) Greenland subglacial drainage evolution regulated by weakly connected regions of the bed. *Nature communications*, **7**(1), 13903 (doi: 10.1038/ncomms13903)

Hoffman MJ, Perego M, Price SF, Lipscomb WH, Zhang T, Jacobsen D, Tezaur I, Salinger AG, Tuminaro R and Bertagna L (2018) MPAS-Albany Land Ice (MALI): a variable-resolution ice sheet model for Earth system modeling using Voronoi grids. *Geoscientific Model Development*, **11**(9), 3747–3780 (doi: 10.5194/gmd-11-3747-2018)

How P, Abermann J, Ahlstrøm A, Andersen S, Box JE, Citterio M, Colgan W, RS F, Karlsson N, Jakobsen J, Langley K, Larsen S, Mankoff K, Pedersen A, Rutishauser A, Shield C, Solgaard A, van As D, Vandecrux B and Wright P (2022) PROMICE and GC-Net automated weather station data in Greenland (doi: 10.22008/FK2/IW73UU)

Irarrazaval I, Werder MA, Huss M, Herman F and Mariethoz G (2021) Determining the evolution of an alpine glacier drainage system by solving inverse problems. *Journal of Glaciology*, **67**(263), 421–434 (doi: 10.1017/jog.2020.116)

Joughin I, Das SB, King MA, Smith BE, Howat IM and Moon T (2008) Seasonal speedup along the western flank of the Greenland Ice Sheet. *Science*, **320**(5877), 781–783 (doi: 10.1126/science.1153288)

Kamb B (1987) Glacier surge mechanism based on linked cavity configuration of the basal water conduit system. *Journal of Geophysical Research: Solid Earth*, **92**(B9), 9083–9100 (doi: 10.1029/JB092iB09p09083)

King MD, Howat IM, Candela SG, Noh MJ, Jeong S, Noël BPY, van den Broeke MR, Wouters B and Negrete A (2020) Dynamic ice loss from the Greenland Ice Sheet driven by sustained glacier retreat. *Communications Earth & Environment*, **1**(1), 1 (doi: 10.1038/s43247-020-0001-2)

Koziol CP and Arnold N (2018) Modelling seasonal meltwater forcing of the velocity of land-terminating margins of the Greenland Ice Sheet. *The Cryosphere*, **12**(3), 971–991 (doi: 10.5194/tc-12-971-2018)

Moody LF (1944) Friction factors for pipe flow. *Trans. Asme*, **66**, 671–684 (doi: 10.1115/1.4018140)

Moon T, Joughin I, Smith B, Van Den Broeke MR, Van De Berg WJ, Noël B and Usher M (2014) Distinct patterns of seasonal Greenland glacier velocity. *Geophysical Research Letters*, **41**(20), 7209–7216 (doi: 10.1002/2014GL061836)

Morlighem M, Williams CN, Rignot E, An L, Arndt JE, Bamber JL, Catania G, Chauché N, Dowdeswell JA, Dorschel B and others (2017) BedMachine v3: Complete bed topography and ocean bathymetry mapping of Greenland from multibeam echo sounding combined with mass conservation. *Geophysical Research Letters*, **44**(21), 11–051 (doi: 10.1002/2017GL074954)

Murray T and Clarke GKC (1995) Black-box modeling of the subglacial water system. *Journal of Geophysical Research: Solid Earth*, **100**(B6), 10231–10245 (doi: 10.1029/95JB00671)

Muthyala R, Rennermalm ÅK, Leidman SZ, Cooper MG, Cooley SW, Smith LC and Van As D (2022) Supraglacial streamflow and meteorological drivers from southwest Greenland. *The Cryosphere*, **16**(6), 2245–2263 (doi: 10.5194/tc-16-2245-2022)

Nienow PW, Sole AJ, Slater DA and Cowton TR (2017) Recent advances in our understanding of the role of meltwater in the Greenland Ice Sheet system. *Current Climate Change Reports*, **3**, 330–344 (doi: 10.1007/s40641-017-0083-9)

Pohle A, Werder MA, Gräff D and Farinotti D (2022) Characterising englacial R-channels using artificial moulins. *Journal of Glaciology*, **68**(271), 879–890 (doi: 10.1017/jog.2022.4)

Poinar K and Andrews LC (2021) Challenges in predicting Greenland supraglacial lake drainages at the regional scale. *The Cryosphere*, **15**(3), 1455–1483 (doi: 10.5194/tc-15-1455-2021)

Poinar K, Dow CF and Andrews LC (2019) Long-term support of an active subglacial hydrologic system in Southeast Greenland by firn aquifers. *Geophysical Research Letters*, **46**(9), 4772–4781 (doi: 10.1029/2019GL082786)

Rada Giacaman CA and Schoof C (2023) Channelized, distributed, and disconnected: spatial structure and temporal evolution of the subglacial drainage under a valley glacier in the Yukon. *The Cryosphere*, **17**(2), 761–787 (doi: 10.5194/tc-17-761-2023)

Röthlisberger H (1972) Water pressure in intra-and subglacial channels. *Journal of Glaciology*, **11**(62), 177–203 (doi: 10.3189/S0022143000022188)

Schoof C (2010) Ice-sheet acceleration driven by melt supply variability. *Nature*, **468**(7325), 803–806 (doi: 10.1038/nature09618)

Schoof C, Hewitt IJ and Werder MA (2012) Flotation and free surface flow in a model for subglacial drainage. Part 1. Distributed drainage. *Journal of Fluid Mechanics*, **702**, 126–156 (doi: 10.1017/jfm.2012.165)

Smeets PC, Kuipers Munneke P, Van As D, van den Broeke MR, Boot W, Oerlemans H, Snellen H, Reijmer CH and van de Wal RS (2018) The K-transect in west Greenland: Automatic weather station data (1993–2016). *Arctic, Antarctic, and Alpine Research*, **50**(1), S100002 (doi: 10.1080/15230430.2017.1420954)

Smith LC, Chu VW, Yang K, Gleason CJ, Pitcher LH, Rennermalm AK, Legleiter CJ, Behar AE, Overstreet BT, Moustafa SE and others (2015) Efficient meltwater drainage through supraglacial streams and rivers on the southwest Greenland ice sheet. *Proceedings of the National Academy of Sciences*, **112**(4), 1001–1006 (doi: 10.1073/pnas.1413024112)

Sommers A, Rajaram H and Morlighem M (2018) SHAKTI: subglacial hydrology and kinetic, transient interactions v1.0. *Geoscientific Model Development*, **11**(7), 2955–2974 (doi: 10.5194/gmd-11-2955-2018)

Stone DB and Clarke GKC (1993) Estimation of subglacial hydraulic properties from induced changes in basal water pressure: a theoretical framework for borehole-response tests. *Journal of Glaciology*, **39**(132), 327–340 (doi: 10.3189/S0022143000015999)

Tsai VC and Rice JR (2010) A model for turbulent hydraulic fracture and application to crack propagation at glacier beds. *Journal of Geophysical Research: Earth Surface*, **115**(F3) (doi: 10.1029/2009JF001474) van de Wal RSW, Greuell W, van den Broeke MR, Reijmer CH and Oerlemans J (2005) Surface mass-balance observations and automatic weather station data along a transect near Kangerlussuaq, West Greenland. *Annals of Glaciology*, **42**, 311–316 (doi: 10.3189/172756405781812529)

van de Wal RSW, Smeets CJPP, Boot W, Stoffelen M, van Kampen R, Doyle SH, Wilhelms F, van den Broeke MR, Reijmer CH, Oerlemans J and Hubbard A (2015) Self-regulation of ice flow varies across the ablation area in south-west Greenland. *The Cryosphere*, **9**(2), 603–611 (doi: 10.5194/tc-9-603-2015)

Venkataraman P and Rao PRM (1998) Darcian, transitional, and turbulent flow through porous media. *Journal of hydraulic engineering*, **124**(8), 840–846 (doi: (ASCE)0733-9429(1998)124:8(840))

Vijay S, King MD, Howat IM, Solgaard AM, Khan SA and Noël B (2021) Greenland ice-sheet wide glacier classification based on two distinct seasonal ice velocity behaviors. *Journal of Glaciology*, **67**(266), 1241–1248 (doi: 10.1017/jog.2021.89)

Ward JC (1964) Turbulent flow in porous media. *Journal of the hydraulics division*, **90**(5), 1–12 (doi: 10.1061/JYCEAJ.0001096)

Werder MA, Loye A and Funk M (2009) Dye tracing a jökulhlaup: I. Subglacial water transit speed and water-storage mechanism. *Journal of Glaciology*, **55**(193), 889–898 (doi: 10.3189/002214309790152447)

Werder MA, Hewitt IJ, Schoof CG and Flowers GE (2013) Modeling channelized and distributed subglacial drainage in two dimensions. *Journal of Geophysical Research: Earth Surface*, **118**(4), 2140–2158 (doi: 10.1002/jgrf.20146)

Wood BD, He X and Apte SV (2020) Modeling turbulent flows in porous media. *Annual Review of Fluid Mechanics*, **52**, 171–203 (doi: 10.1146/annurev-fluid-010719-060317)

Wright PJ, Harper JT, Humphrey NF and Meierbachtol TW (2016) Measured basal water pressure variability of the western Greenland Ice Sheet: Implications for hydraulic potential. *Journal of Geophysical Research: Earth Surface*, **121**(6), 1134–1147 (doi: 10.1002/2016JF003819)

Yang K and Smith LC (2016) Internally drained catchments dominate supraglacial hydrology of the southwest Greenland Ice Sheet. *Journal of Geophysical Research: Earth Surface*, **121**(10), 1891–1910 (doi: 10.1002/2016JF003927)